Observable Properties of the Breakout Model for Coronal Mass Ejections

B. J. Lynch[1,2]

lynchb@engin.umich.edu

S. K. Antiochos[1,2]

antiochos@nrl.navy.mil

P. J. MacNeice[3]

macneice@alfven.gsfc.nasa.gov

T. H. Zurbuchen[1]

thomasz@umich.edu

L. A. Fisk[1]

lafisk@umich.edu

ABSTRACT

We compare the "magnetic breakout" model for coronal mass ejections (CMEs) to observed general properties of CMEs by analyzing, in detail, recent high-resolution MHD simulations of a complete breakout CME. The model produces an eruption with a 3-part plasma density structure that shows a bright circular rim outlining a dark central cavity in synthetic coronagraph images of total brightness. The model also yields height-time profiles similar to most 3-part CMEs, but the eruption speed by 2.5 $R_\odot$ is of order the Alfven speed, indicative of a fast CME. We show that the evolution of the post-eruptive flare loop and chromospheric ribbons determined from the model are in agreement with observations of long-duration flares, and we propose an explanation for the long-standing observation that flares have an impulsive and gradual phase. A helical

[1]Department of Atmospheric, Oceanic, and Space Sciences, University of Michigan, Ann Arbor, MI, 48109

[2]E. O. Hulburt Center for Space Research, Naval Research Laboratory, Washington, DC, 20375

[3]Department of Physics, Drexel University, Philadelphia, PA, 19104

magnetic flux rope is generated during eruption and is consistent with a large class of interplanetary CME observations. The magnetic fields in this flux rope are well-approximated by the Lundquist solution when the ejecta is at 15 $R_\odot$ and beyond. Furthermore, the interior density structure of the magnetic flux rope appears to have some of the basic features of an "average" magnetic cloud profile at 1 AU. Future simulation improvements and more stringent observational tests are discussed.

Subject headings: MHD — Sun: corona — Sun: coronal mass ejections (CMEs) — Sun: magnetic fields

1. Introduction

A convincing link between erupting prominences and the classic 3-part CMEs has been established by numerous observations (e.g. Dere et al. 1999; Plunkett et al. 2000). An equally convincing link between 3-part CMEs and interplanetary flux ropes is currently being established by a wide variety of modeling. Many of the observational signatures of CME models have been presented with varying levels of agreement with data, but typically with emphasis on only one or two regimes of observations. There has been relatively good agreement to solar prominence observations (Amari et al. 2000, 2003), white-light coronagraph images (Gibson & Low 1998; Chen et al. 2000; Manchester et al. 2004a), coronal height-time profiles (Krall et al. 2001; Linker et al. 2002; Manchester et al. 2004a), and interplanetary magnetic field measurements (Wu et al. 1999; Riley et al. 2003; Manchester et al. 2004b). However, no model or simulation has yet demonstrated consistency with *all* the observational regimes from the solar surface to 1 AU.

The breakout model for CME initiation and acceleration has attracted considerable attention in recent years (Antiochos 1998; Antiochos, DeVore, & Klimchuck 1999; DeVore & Antiochos 2000; Aulanier, DeVore, & Antiochos 2002). Its main features are that the energy source for the eruption, the non-potential magnetic field of a filament channel, is simply a sheared arcade, and that reconnection above the filament channel causes the eruption. Through detailed analysis of multiple data sets, including line-of-sight and vector magnetograms, EUV, soft X-ray, and radio observations, the magnetic field topology, its evolution, and the coronal responses required for the breakout CME scenario appear to be confirmed for several solar events (e.g. Aulanier et al. 2000; Sterling & Moore, 2001, 2004; Wang et al. 2002; Manoharan & Kundu 2003). Even the energy buildup process, photospheric shear localized at an active region neutral line, has been observed recently by Welsch et al. (2004) in the evolution of AR 8210 prior to an eruption.

Previous work, however, has consisted primarily of searching for the defining features of the model in particular events, rather than a quantitative analysis of the observables predicted by the model. In this paper, we analyze in detail the latest simulations of breakout by MacNeice et al. (2004), and demonstrate that the model is in agreement with all the major properties of CME observations from the low corona through interplanetary space. Section two describes briefly the breakout model and the details of the numerical simulation. Section three focuses on the morphology and dynamics of the CME and comparisons to coronagraph observations. Section four details the calculated flare loop and chromospheric ribbon dynamics. Section five presents our indirect comparison with in-situ measurements, showing field and density structures consistent with data. In section six we conclude with a discussion of future simulation improvements and additional observational tests.

2. Model Description

A full description of the motivation, theory, and energetics of the magnetic breakout model for CME initiation can be found in Antiochos et al. (1999), but for completeness, we briefly review the model's mathematical details that are critical to our subsequent analysis. We also describe the simulation results, including the details of various phases of the breakout eruption before analyzing each of these phases for their relavent observational properties. A comprehensive treatment of the MHD simulation's technical/numerical intricacies can be found in MacNeice et al. (2004).

2.1. Simulation Details and Initial Conditions

The 2.5D simulation is run in a spherical-polar coordinate system (r, θ) with the *ARMS* (Adaptively Redefined MHD Solver) code. The velocity and magnetic field vectors can have non-zero $\hat{\phi}$ components, but the simulation has azimuthal symmetry. *ARMS* solves the time-dependent MHD equations on a dynamically, solution-adaptive grid. The code uses modified flux-corrected transport (FCT) algorithms (DeVore 1991) and the adaptive mesh toolkit, *PARAMESH* (MacNeice et al. 2000). Rather than focusing the numerical resolution only on the current sheets at the reconnection sites as in MacNeice et al. (2004), the particular run presented in this paper has fixed, uniform refinement in order to resolve, as accurately as possible, the structure and evolution of the ejected plasmoid out to large radii. We are more interested in the large-scale structure and development of the eruption than in its initiation. The simulation uses a 512×1024 uniform grid in $\log(r), \theta$. Note that the runs reported by MacNeice et al. (2004) have this level of resolution only in regions

where the grid is at the highest refinement level. Of course, there is a heavy computational penalty for using a highly refined grid everywhere, therefore, in order to keep the total run time at an acceptable level, we drove the system with a shearing velocity a factor of 4 higher than in the MacNeice et al. (2004) runs. However, the maximum shearing velocity is still $<$40 km s^{-1} (only $\sim$10 % of the coronal Alfven speed) and the results resemble closely the slower sheared case. The faster driving causes the system to erupt at an earlier time, but the eruption occurs at approximately the same magnetic energy, and there is no significant effect on the structure or speed of the eruption. MacNeice et al. (2004) ran identical cases for various grid sizes and driving and found that the speed of the eruption is quite insensitive to the parameters of the simulation.

The 2.5D geometry is the same as that of Antiochos et al. (1999), except the computational domain extends to $r = 30\mathrm{R}_\odot$. The simulation is run until $t \sim$60,000 seconds at which point the center of the plasmoid has reached $\sim$15 $\mathrm{R}_\odot$ and the leading shock, $\sim$20 $\mathrm{R}_\odot$. This ensures that the outer boundary conditions do not influence the solution.

Figure 1 shows the initial magnetic topology and its subsequent evolution during a breakout eruption. The initial state shown in (a) has four distinct flux systems: a central arcade overlying the equator, two arcades associated with neutral lines at $\pm$ 45° and a global dipole. There are two separatrix surfaces defining the boundaries between the various flux systems and a null point at the equatorial intersection of these separatricies. The initial, unstressed (potential) field (in polar coordinates r, θ) is given by

$$A(r,\theta) = \frac{\sin^2\theta}{r} + \frac{(3+5\cos 2\theta)\sin^2\theta}{2r^3}. \tag{1}$$

The dipole component dominates at large r and the octopole component contributes primarily to the complex multi-flux system near the surface.

We increase the magnetic energy of the pre-eruption state by applying a boundary flow which produces a shear in the field near the neutral line. The flow at the boundary is applied only to the innermost half, approximately, of the equatorial flux system. The shearing profile is antisymmetric about the equator and is given by

$$\gamma(r = 1\mathrm{R}_\odot, \theta) = \begin{cases} V_0(\psi^2 - \Theta^2)^2 \sin\psi & \text{if } \psi < \Theta, \\ 0 & \psi \geq \Theta, \end{cases}$$

such that $\psi \equiv \frac{\pi}{2} - \theta$ is the solar latitude, $\Theta = \pi/15$ is latitudinal extent of the applied shear on either side of the neutral line, and V_0 is a normalization constant. This flow is imposed with a sinusoidal time dependence, $\sin(\pi t/\tau)$, where $\tau = 25,000$ s, and the flow is turned off for $t > \tau$.

The simulation has an initial equilibrium density and temperature profile of

$$n(r) = \frac{2 \times 10^8}{r^7} \text{ cm}^{-3}, \quad T(r) = \frac{2 \times 10^6}{r} \text{ K}, \tag{2}$$

and starts at rest, $\mathbf{u}(r, \theta) = 0$. This density and temperature profile where chosen to compensate for the rapid decrease in magnetic field strength, so that the plasma β ($= 8\pi nkT/B^2$) does not become too large at large distances from the sun. Note that this initial state does not contain any additional cool mass corresponding to a prominence. During the shearing phase, we expect the simulation to be a good representation of prominence fields because the magnetic topology of a low-lying sheared arcade has shown excellent agreement with field structures inferred from both quiescent and erupting prominence observations (DeVore & Antiochos 2000). In section three, we will show that even without additional prominence mass, the simulation produces a 3-part CME density structure including the central core most often associated with eruptive prominences. Although rare, there have been a couple observations of CMEs with core structures that do not appear to be associated with eruptive prominence material (e.g. Gilbert et al. 2000).

2.2. Eruption Timeline

All phases of the magnetic breakout eruption can be seen in figures 1 and 2. Figure 1 shows the initial field configuration and its evolution during the shearing and eruption phases. The density images in figure 2 (left column) pick up where figure 1 leaves off, following the ejecta's development to large radii.

At $t = 0$ the shearing is turned on. We ramp the shear up and down simusoidally over a total duration of 25,000 seconds, i.e. through Figure 1 (d), but the eruption occurs well before this time. The effect of turning on the shear is to add magnetic pressure to the inner-flux system, which causes it to expand and distort the overlying null-point, eventually stretching it to a thin current sheet, shown in panel (b).

By $t = 20,000s$ the current sheet thickness has becomes of order a few grid cells, causing numerical diffusion to kick in and, consequently, the breakout reconnection to start. As is evident by comparing Figures 1 (c) and (b), the reconnection transfers some of the restraining overlying flux to the side lobes. The loss of restraining field produces a noticeable increase in the rate of outward expansion; therefore, we define the onset of breakout reconnection, $t = 20,000s$, to be the start the eruption. The rapid expansion, in turn, drives a faster rate of breakout reconnection, yielding the positive feedback that is required for explosive eruption (Antiochos et al. 1999). The large expansion also leads to the formation of a

radially-oriented current sheet deep inside the inner flux system, as can be seen in Figure 1 (d) through (e).

By $t = 23,000s$, the width of the inner current sheet decreases to the grid scale and reconnection begins there. This inner sheet and the reconnection there correspond to the vertical current sheet and reconnection in the standard model for eruptive two-ribbon flares; hence, $t = 23,000s$ can be considered to mark the start of the flare impulsive phase described in section 4 and shown in panel (d) as well as figure 5. An intriguing point is that the flare reconnection first appears in the sheared-field region, indicating that at least initially, the flare impulsive phase corresponds to the reconnection of stongly-sheared field.

By $t = 28,000s$ all the sheared flux has been processed though the flare current sheet, and the flare reconnection progresses into the unsheared-field region. As discussed in more detail below, we conjecture that this transition corresponds to the end of the flare impulsive phase. In addition to building up the flare loop system in the low corona, it is evident from Figure (1) that the flare reconnection also disconnects flux from the solar surface (in 2.5D only), thus transforming the erupting sheared arcade into a flux rope structure, which is ejected into the heliosphere, panel (f).

By $t = 32,000s$, all the field remaining in the inner flux system has been processed through the flare reconnection, and the ejected rope reaches its maximum flux. But this is not the end of the flare reconnection, which continues until well beyond $t = 40,000s$. The source for this continued flare reconnection is the side lobes, which have grown substantially from their initial potential state due to the breakout reconnection. After the ejection of the flux rope, the side lobes push together at the inner current sheet allowing the flare reconnection there to rebuild the inner and outer flux systems. It is interesting to note that when the side lobes begin to reconnect, a new pair of ribbons should appear. This can be seen by studying the last panel of Figure 1. When the two side lobes reconnect at the equatorial current sheet, they will produce ribbons both at their inside boundaries, corresponding to the flare ribbons, and at their outside boundaries, corresponding to new, distant ribbons. Hence, one prediction of the breakout model is the appearance of new ribbons during the flare main phase.

Figure 2 shows number density during the late development phase of the eruption. The evolution is dominated by the rapid expansion of the ejecta. Breakout magnetic reconnection at the outermost X-point is still occuring, but acts primarily to move the ejected flux rope through the overlying dipole flux system. During this late phase the total flux in the ejected rope actually decreases slightly as a result of the breakout reconnection. The important feature of Figure 2 is that at these distances from the Sun, the simulation results can be compared with coronagraph observations.

3. Coronagraph Comparisons

3.1. Coronagraph Morphology

The white-light C2 and C3 Large Angle Spectrometric Coronagraphs (LASCO; Brueckner et al. 1995) aboard the *Solar and Heliospheric Observatory* (SOHO) spacecraft have provided an immense archive of detailed observations of solar transients. While there are numerous CME morphologies in the coronagraph observations, we are most interested in the one thought to be associated with both erupting prominences and interplanetary magnetic cloud observations: the classic 3-part CME (e.g. Dere et al. 1999). The 3-part CME has a white-light intensity (line-of-sight integrated density) structure made up of a loop-like initial enhancement followed by a large tenuous cavity with a bright central core (Illing & Hundhausen 1986; Hundhausen 1999). The prominence material is most commonly associated with the central core, while the less dense cavity region is assumed to contain the stronger fields of a flux rope seen end on. In fact, this is exactly what the simulation shows (for example, see figures 5, 7). We have created synthetic, background-subtracted white-light coronagraph images from the simulation density structure, demonstrating the breakout model reproduces both the bright loop and dark cavity of the common observational signature of 3-part CMEs.

The left column of figure 2 shows the density structure at various times during the breakout simulation. The right column shows the corresponding CME contribution to white-light coronagraph images. This is the scaled, relative total brightness intensity, defined as

$$\delta I_B(t) = K\left(I_B(t) - I_B(0)\right). \tag{3}$$

Here $K = I_B(0)^{-1}$ is the scaling constant and $I_B(t)$ is calculated by integrating $I_t + I_r$ over the line-of-sight. I_t and I_r are the tangential and radial polarized intensities and are given by the well known Thompson scattering formulas (van de Hulst 1950; Billings 1966; Hayes, Vourlidas, & Howard 2001). The time elapsed from the beginning of the imposed shearing motion is indicated on each panel.

The 3-part density structure is well defined by $t \sim$35,000 seconds. The blurring of the bright rim into the cavity region in the δI_B images is expected from the broad line-of-sight response of a shell-like density enhancement (e.g. Lynch, Coles, & Sheeley 2002). The rim contribution is composed of ambient coronal plasma swept up by the expanding eruption. It is difficult to quantitatively compare the rim brightness with coronagraph data because our density falls off like r^{-7} (to keep the simulation plasma β reasonably low), much faster than the solar wind density. Since the simulation models an active-region type field expanded over the whole sun, the closed-field contribution to the bright rim represents a helmet streamer configuration, which the eruption would blow out.

The evolution of the core is interesting because the tenuous plasma in the central bubble of the CME appears to coalesce during evolution. Even though we do not begin with any dense prominence material in this simulation, a density enhancement forms at the trailing end of the plasmoid's magnetic field lines due to the inertia of the plasma. As the plasmoid accelerates outward, material slides down along the field and collects in the concave-up portion of the field. This core density makes only a small contribution to δI_B because it does not represent much of an enhancement over the background, and with the 2.5D symmetry the cavity is unrealistically extensive (a giant torus encircling the sun). In order to increase the core's contribution to the relative brightness, additional mass representing prominence material could be included in the low-lying pre-eruption, sheared flux region. But it is interesting to note that a filament ejection is not required for a CME to have a distinct 3-part density structure.

3.2. Coronagraph Dynamics

The cadence of the LASCO instruments is sufficient to measure, in detail, the dynamics of a CME as it propagates through the 30 $R_\odot$ field of view. Movies of these transient events, their evolution through the corona, and their effect on the existing background structure have provided new insights into the associated physical processes. Height-time plots, typically made from running-difference movies, describe the projected plane-of-the-sky velocity and acceleration profiles. This technique has been used to define the two dynamical types of CMEs based on the shape of their height-time curves (Sheeley et al. 1999). The "slow" CME events have a height-time profile that gradually builds speed toward an asymptotic final velocity, usually the ambient solar wind speed, ∼300-500 km s^{-1}. The "fast" CMEs start at the edge of the C2 occulting disk (2.5 $R_\odot$) with very high speeds, often $>$ 1000 km s^{-1}, and decelerate during their transit through the C3 field of view. Having constructed a running-difference movie of the breakout model density, we can use the same LASCO height-time analysis to compare the simulation to actual CME observations.

Figure 3 shows an image from the running-difference movie with arrows indicating the leading edge of the initial density enhancement, the leading edge of the dark cavity, and the leading edge of the central core. The top panel of figure 4 plots the height-time tracks from the running-difference movies in the style of Sheeley et al. (1999) figures. The lower panel plots the same data as points with the solid lines showing quadratic fits to the height-time data of the form

$$r(t) = r_0 + v_0(t - t_0) + \tfrac{1}{2}a_0(t - t_0)^2 \tag{4}$$

The constant accelerations were 8.9, 8.0, and 4.2 m s^{-2} for the CME Front, Cavity, and Core

running-difference features respectively. From these fits, the final velocities are 466.9 km s^{-1} for the CME Front, 377.3 km s^{-1} for the Cavity, and 266.7 km s^{-1} for the Core.

All three of these curves show the characteristic shape of "slow" CMEs. A large majority of the observations of 3-part CMEs and those inferred to contain helical field structure have the "slow" CME profile (Dere et al. 1999; Sheeley et al. 1999; Krall et al. 2001). This result may seem unexpected, because the breakout model was originally proposed as an explanation for fast eruptions (Antiochos 1998; Antiochos et al. 1999). However, the actual eruption speed is consistent with fast eruptions. For this particular simulation, the maximum Alfven speed is approximately 450 km s^{-1}. We note the inferred CME Front final velocity also reaches this speed. Furthermore, in the numerical studies of MacNeice et al. (2004), the magnetic field strength of the system was increased by an order of magnitude and both the Alfven speed and ejecta velocities exceeded 1000 km s^{-1}. Therefore, it appears that the breakout model does yield a fast CME, but that the time scale for the acceleration, several hours, is more typical of a slow eruption.

The origin of this discrepancy is due primarily to the spatial scale of the initial magnetic field. In order to maximize the effective numerical resolution, we chose a field that has a scale of order the whole Sun. But fast CMEs originate from active regions which have scales at least an order of magnitude smaller. We expect that if we were to shrink the size of our multi-polar field structure down to active region scales (and increase the field strength appropriately), the resulting CME would be fast and would reach its maximum velocity well below 2.5 $R_\odot$. Also, to match in detail the two dynamical height-time shapes seen in the coronagraph observations, a background solar wind would have to be included. This would allow a fast breakout eruption to show the characteristic deceleration as it plows into the slower moving material ahead of it, as well as a slower, weaker field eruption to accelerate to the background wind speed.

4. Post-Eruption Flare Loop and Ribbon Dynamics

An important feature of the simulation is that the eruption leads to the formation of a radial current sheet along the equatorial plane and, consequently, to reconnection deep inside the core of the sheared flux. This inner current sheet results directly from the large outward expansion of the field, and is a general feature of every simulation of eruption (e.g. Mikic & Linker 1994). If the field were to open up without reconnecting, the final state would have an equatorial current sheet extending from very near the inner boundary out to infinity (Antiochos et al. 1999). But due to the presence of numerical diffusion in the code, the fields start reconnecting almost as soon as the current sheet begins to form, closing the field back

down to a more potential state. In 2D, the inner reconnection forms a disconnected plasmoid that escapes the corona. We expect that in 3D the plasmoid would not be truly disconnected, instead it would correspond to a highly twisted flux rope connected at both ends to the solar surface (Gosling, Birn, & Hesse 1995). The basic picture would be unchanged, i.e. our 2D results would likely correspond to the central meridional cut of a truly 3D ejection. However, maintaining this 3D ejecta-solar connection for the entire propagation to 1 AU may prove to be numerically challenging (e.g. Manchester et al. 2004b).

It should be emphasized that the reconnection at the equatorial current sheet is completely distinct from the breakout reconnection at the coronal null. It corresponds to the post-eruption flare reconnection as described in the classical model for two-ribbon flares (Carmichael 1964; Sturrock 1968; Hirayama 1974; Kopp & Pneuman 1976). The breakout reconnection allows the field to open, whereas the flare reconnection closes the field back down. Flare reconnection has been studied in many simulations (e.g. Forbes & Malherbe 1991; Shibata, Nozawa, & Matsumoto 1992; Yokoyama & Shibata 1996; Magara et al. 1996), but these calculations generally begin with a pre-existing vertical current sheet. A key feature of the simulation presented in this paper is that it provides a self-consistent calculation of both the formation and reconnection of the flare current sheet. Therefore, we are able to compare the results of our model with observations of both flare rise and decay.

Although the actual flare current sheet and reconnection region have yet to be identified definitively in the observations, there are two well-accepted observations of the consequences of flare reconnection: the growing arcades of 10 MK coronal loops observed in X-rays and the spreading chromospheric ribbons observed in H_α. In the classical flare model, the X-ray loops are presumed to correspond to newly-formed closed flux tubes that have been heated by the reconnection process, and the ribbons are simply the chromospheric footpoints of those loops. Since our simulation uses only an ideal energy equation and does not include processes such as chromospheric evaporation, we cannot predict flare plasma temperatures and densities for comparison with data, but we are able to calculate accurately the growth of the coronal loops and the separation of the corresponding footpoint ribbons.

An appropriate measure for the height of the flare loops is the location along the equator of the lowest null-point in the equatorial current sheet. The field lines traced from this null point define the upper boundary of the flare loop system – the separatrix between the closed field lines and the erupting plasmoid. The ribbon separation can then be measured directly by calculating the arc length between the two footpoints on the photosphere of the separatrix lines. Figure 5 shows a close-up view of the field lines and number density beneath the erupting flux rope. The equatorial current sheet is clearly visible. The dotted lines on the solar disk indicate the footpoints of the azimuthally symmetric two-ribbon flare.

The top panel of figure 6 shows the simulation flare loop arcade height vs time. The second panel shows the evolution of the footpoint (ribbon) separation of the post-flare loop system with time. Our breakout simulation yield profiles that appear very similar to decades of flare loop height observations on the limb (Moore et al. 1980; van Driel-Gesztelyi et al. 1997; Ko et al. 2003) and flare ribbon separation on disk center (Moore et al. 1980; Wang et al. 2003). We note that while the flare loop heights increase steady in time throughour the flare, the footpoint separation shows a fast rise at the onset of the current-sheet reconnection, followed by a slowly increasing main phase.

The impulsive phase of a flare is defined by the sharp rise in the soft X-ray flux and bursty hard X-ray emission. Recent observations imply that the main acceleration phase of erupting filaments and CMEs also occur during this period (Zhang et al. 2001; Gallagher et al. 2003; Wang et al. 2003). The CME Front and Cavity height-time profiles from figure 4 are replotted in the last panel of figure 6. The observed temporal relation between the flare impulsive phase and the filament/ejecta acceleration agrees with our simulation results. It is only natural to associate the runaway breakout expansion and subsequent current sheet formation, impulsive ribbon separation, and flux rope formation with the observed CME acceleration phases.

The observation of a short impulsive phase followed by an extended main phase has long been known to be a generic feature of flare energy release (e.g. Sturrock 1980). The standard explanation for the origin of this feature is that it is due to the decrease of magnetic field strength with height, which results in a decrease in the rate of reconnection with height. There is little doubt that this effect must be present to some extent, but it seems unlikely that it is the most important effect. The physical differences between the flare impulsive and main phase are pronounced and the transition from impulsive to main phase is typically abrupt, whereas the field strength must decrease smoothly with height in order to have force balance in the pre-eruption equilibrium. Perhaps, the clearest discriminator between the impulsive and main phases is the observation of non-thermal emission. Hard X-ray bursts are invariably seen only during the impulsive phase (Sturrock 1980). Again, it seems unlikely that a smooth decrease in magnetic field strength would result in an abrupt stop in non-thermal particle production.

We believe that the observed differences between the impulsive and main phases originate from the differences between reconnection in a sheared versus unsheared field. Although the total field strength decreases smoothly with height, the shear component does not. Numerous observations have shown that the shear is invariably concentrated in the filament channel near the neutral line (e.g. Martin 1998; DeVore & Antiochos 2000). To our knowledge, the shear is the only property of the pre-eruption field that exhibits such a

quasi-discontinuous structure and, hence, is the only likely cause for the two phase nature of flares. The transition from rapid to slow ribbon spreading can readily be understood in terms of reconnection with and without shear. Initially, the flare reconnection occurs deep in the strong sheared region and, therefore, produces a plasmoid with a strong B_ϕ component, which greatly enhances the outward magnetic pressure gradient. But, eventually, the filament channel field reconnects fully and the unsheared flux propagates into the reconnection region. The flux subsequently added to the plasmoid has almost no B_ϕ component, and as a result, the outward force begins to level off. To verify this picture, we have plotted the B_ϕ value at the lowest current-sheet null point in the third panel of figure 6. The impulsive phase of the flare has ended after the sheared field has becomes fully reconnected, and this is very close to the transition from fast to slow ribbon spreading.

We believe that the observed cessation of hard X-ray bursts with the start of the main phase can also be understood in terms of the difference between reconnection in a strongly sheared versus unsheared field. The leading candidate for the acceleration of the particles (primarily electrons) that give rise to the hard X-rays is the generation of fast shocks/strong turbulence (e.g. Somov & Kosugi 1997; Miller, LaRosa, & Moore 1996) by the Alfvenic outflows from the reconnection region (Sweet 1958; Parker 1963; Petschek 1964). When the reconnection involves the strongly sheared flux, the outflows will carry a large quasi-perpendicular field component, but when the reconnection occurs in the unsheared field, the outflows will be primarily field aligned. It is well known that quasi-perpendicular shocks/turbulence are much more efficient for electron acceleration than quasi-parallel shocks/turbulence (Giacalone 2003, private communication). Of course, this straightforward idea requires critical testing with detailed calculations, but unfortunately, our present simulations are too diffusive to produce significant strong turbulence/fast shocks in the closed field region. Further simulations which focus on the flare reconnection region are clearly needed.

5. In-Situ Comparisons

In addition to solar observations, the results of our simulation can be indirectly compared with in-situ data at 1 AU. Since the outer computational boundary is only 30 $R_\odot$ and the simulation lacks any sort of background solar wind, a direct comparison to 1 AU measurements is not possible with these results, but will be the subject of future work. However, by examining the flux rope structure close to the sun, we can demonstrate that the internal magnetic field and density structures resemble the general features of interplanetary magnetic cloud observations.

5.1. Flux Rope Magnetic Field Structure

Magnetic clouds are a special, well-ordered type of interplanetary CME. There is an extensive history of magnetic cloud observations and modeling of their flux rope structure. For our comparisons, we will be content to use the simplest, well-proven model (Burlaga 1988; Lepping, Jones, & Burlaga 1990). This simple field model is the Lundquist (1950) solution to the force-free magnetic field equation $\nabla \times \mathbf{B} = \alpha \mathbf{B}$. In cylindrical coordinates, it yields field components

$$\mathbf{B} = H B_0 J_1(\alpha\rho)\hat{\phi} + B_0 J_0(\alpha\rho)\hat{z}. \tag{5}$$

Here B_0 is the field magnitude on the cylinder symmetry axis, ρ is the distance from the axis, α is the constant force-free parameter, related to the magnetic helicity, and H is its sign. J_0, J_1 are the zeroth and first order Bessel functions. Defining the outer edge of the cloud as the first zero of J_0 constrains α such that $\alpha R_c = x_{01} \simeq 2.405$.

The general success of modeling the field rotation within these magnetic clouds has motivated and enabled researchers to identify the solar origin of these special kinds of CMEs (e.g. Bothmer & Schwenn 1994, 1998; Rust 1994, 1999; Marubashi 1997). From the magnetic field signatures there is a fairly well-established relationship between erupting prominences, their associated CMEs, and interplanetary flux ropes. The breakout model generates a flux rope structure by reconnection during the eruption. This flux rope exhibits excellent agreement with the field structure of interplanetary magnetic cloud observations.

The left panel of figure 7 shows the breakout simulation at $t = 56,936$ seconds. The colorscale is again number density [cm^{-3}] and the meridional projections of the helical flux rope fieldlines are over-plotted. The points through the flux rope indicates the spatial sampling of the simulation magnetic field, plotted in figure 8 (solid lines). The right panel of figure 7 shows a few representative field lines from the linear, force-free (LFF) cylinder model for magnetic clouds given by equation 7. This model is also plotted in figure 8 for comparison with the simulation data (dotted lines). The cylinder parameters are $\phi_0 = 90°, \theta_0 = 0°, \rho_0 = 0, H = -1$, and $B_0 = 0.008$ G. The two angles describe the symmetry axis orientation with respect to the ecliptic plane, i.e. the cylindrical axis is perpendicular to the page of figure 7. The impact parameter $|\rho_0|$ indicates the minimum distance between the sampling trajectory and the cylinder axis normalized to the cylinder radius.

We conclude that the magnetic fields in the interior of the breakout flux rope are well approximated by the LFF model that has described interplanetary flux rope observations so successfully. The fact that this approximation works so close to the sun implies that most of the internal reconnection and/or diffusion required to drive the twisted fields toward a linear force-free state has happened by 15 $\mathrm{R}_\odot$.

It should be emphasized, however, that the flux rope evolution from 15 $R_\odot$ to 1 AU is by no means trivial. Recent results from the University of Michigan employing adaptive block-structured grids (Manchester et al. 2004a,b) and the SAIC-NOAA/SEC collaboration using coupled coronal and heliospheric computational domains (Odstrcil et al. 2002; Riley et al. 2003) have both shown significant deformation of the original flux rope structure during propagation through the heliosphere. Manchester et al. (2004b) have a smooth transition to high speed solar wind over the poles, resulting in a substantial velocity gradient throughout the flux rope. As the flux rope expands into higher and lower latitude regions the velocities pull the original circular cross section into a left-parenthesis shape, "(", because the Alfven speed is slowest at the current sheet, corresponding to the center of the flux rope. On the other hand, Riley et al. (2003) describe their 1 AU flux rope structure as a pancake, having deformed from the original elliptical shape into a right-parenthesis shape, ")", due largely to the lack of a major latitudinal solar wind velocity gradient in their simulation. However, in both cases, the fields from synthetic spacecraft trajectories at many different latitudes are well approximated by LFF cylinder fits even if there is sometimes significant discrepancies between the true simulation geometry and the cylinder fit orientation (e.g. Riley et al. 2004). Our results indicate that the LFF approximation may be valid even when the flux rope is quite near the Sun.

5.2. Flux-Rope Density Structure

The interior density structure of the breakout flux rope can be compared to an average density profile of magnetic cloud events observed at 1 AU. Figure 9 shows eight diameter-sampling trajectories in a star-type pattern that intersect the center of the magnetic flux rope. Note we are sampling just the disconnected plasmoid region of the larger CME structure. In order to simulate the mass diffusion along concentric fieldlines, each diameter cut was divided into two radial cuts and the 16 radial density profiles were averaged to create a symmetric, average radial flux rope density profile. This is plotted as the upper panel of figure 10.

Lynch et al. (2003) have constructed a similar profile from 56 magnetic clouds events observed by the *Advanced Composition Explorer* (ACE) spacecraft. This technique uses the geometry of the linear, force-free model described in the previous section to map plasma measurements to a spatial location within the model cylinder. The lower graph of figure 10 shows two composite average diameter profiles for magnetic clouds observed at 1 AU. There are two profiles plotted because the interior ionic composition differed greatly between clouds of different speeds. The "slow" profile is a composite average of the 42 magnetic clouds with

event-averaged radial velocity $\langle V_r \rangle < 500$ km s^{-1} while the "fast" profile is an average of the 14 clouds with $\langle V_r \rangle \geq 500$ km s^{-1}.

The general likeness between the overall shape of the simulation density average and the leading or trailing halves of the 1 AU magnetic cloud averages is immediately apparent. The simulation interior sinusoidal structure (the peak at $\sim 0.5 R_c$) comes from the ring-like density enhancement that develops during the core region evolution. This is most easily seen in the last two panels of figure 2. Furthermore, the magnitude of the breakout simulation average density range, approximately $1000 - 1500$ cm^{-3}, scaled by $1/r^2$ from 15 to 215 R$_\odot$ gives values of $4.9 - 7.3$ cm^{-3}, which matches the ACE magnetic cloud averages extremely well. It is not clear, however, if this agreement would continue to hold if we were to use an active region scale magnetic topology for the breakout simulation or if this sinusoidal density structure would survive the transit to 1 AU.

6. Conclusions

The main conclusion from the results above is that the breakout model for coronal mass ejection initiation passes the first round of observational tests. The success of the breakout model in reproducing a broad range of large-scale observational characteristics is encouraging. Our results demonstrate that a pre-existing flux rope is not necessary for reproducing coronagraph and in-situ observations of helical field structures, as we have shown that the generation of this field structure by magnetic reconnection *during* the eruption, is also consistent with CME observations. The breakout simulation produces a 3-part density structure with the bright rim and dark cavity features in synthetic coronagraph images, the most common height-time plot for 3-part CMEs with final velocities controlled by the Alfven speed of the numerical simulation, post-eruptive flare dynamics with the observed characteristics, and even a linear, force-free flux rope very close to the sun.

The main weakness of our numerical simulation is that it does not include enough physics in the energy equation to permit accurate calculation of the plasma thermal properties. There is no background solar wind (or its associated heating) and no accounting for the transfer of magnetic energy to plasma thermal energy through reconnection. With simulation improvements such as the energy transport terms of volumetric heating, field-aligned conduction, and radiative cooling, future CME/eruptive flare simulations could be compared to actual flare loop temperatures and densities. Further more, in-situ heavy ion charge states have become an important tool for "remote sensing" the thermal conditions in the low corona because these charge states are frozen into the solar wind (or CME material), typically < 4 R$_\odot$. Interplanetary CMEs are often associated with unusual charge state composition,

and the thermal properties and spatial distribution of reconnection-heated plasma may be one of the distinguishing features of various models for CME initiation.

Another major conclusion of our work is that much remains to be done. Despite all the observational agreements presented herein, the model is only axisymmetric and the initial magnetic geometry is highly idealized. A full 3D treatment is clearly required before realistic comparisons to observations and integration of data into the model boundary conditions can be made. Our results also highlight one of the fundamental puzzles in solar and heliospheric physics. Why are most interplanetary CMEs not magnetic clouds? We have shown that the breakout model, like basically all CME models, produces a Lundquist-like flux rope. We do not expect this result to change significantly in 3D. It seems clear, therefore, that not only the initiation process, but the propagation and interaction of CMEs with the solar wind require further theoretical and observational study.

This work was supported, in part, by NASA, ONR, and the NSF. BJL is supported by a NASA GSRP fellowship NGT5-50453. The authors would like to thank N. Sheeley for assistance with the LASCO/simulation height-time analysis. This work greatly benefited from discussions at the NSF SHINE Workshops.

REFERENCES

Amari, T., Luciani, J. F., Mikic, Z., & Linker, J. A. 2000, ApJ, 529, L49

Amari, T., Luciani, J. F., Aly, J. J., Mikic, Z., & Linker, J. A. 2003, ApJ, 585, 1073

Antiochos, S. K. 1998, ApJ, 502, L181

Antiochos, S. K., DeVore, C. R., & Klimchuck, J. A. 1999, ApJ, 510, 485

Aulanier, G., DeLuca, E. E., Antiochos, S. K., McMullen, R. A., & Golub, L. 2000, ApJ, 540, 1126

Aulanier, G., DeVore, C. R., & Antiochos, S. K. 2002, ApJ, 567, L97

Billings, D. E. 1966, A Guide to the Solar Corona, New York, Academic Press

Birn, J., J. T. Gosling, M. Hesse, T. G. Forbes, & E. R. Priest, ApJ, 541, 1078

Bothmer, V., & Schwenn, R. 1994, Space Sci. Rev., 70, 215

——. 1998, Ann. Geophysicae, 16, 1

Brueckner, G. E., et al. 1995, Sol. Phys., 162, 357

Burlaga, L. F. 1988, J. Geophys. Res., 93, 7217

Carmichael, H. 1964, in Proc. AAS-NASA Symp., The Physics of Solar Flares, ed. W. N. Hess (NASA SP-50; Washington, DC: NASA), 451

Chen, J., et al. 2000, ApJ, 533, 481

Dere, K. P., Brueckner, G. E., Howard, R. A., Michels, D. J., & Delaboudiniere, J. P. 1999, ApJ, 516, 465

DeVore, C. R. 1991, J. Comput. Phys., 92, 142

DeVore, C. R., & Antiochos, S. K. 2000, ApJ, 539, 954

Forbes, T. G. & J. M. Malherbe, 1986, ApJ, 302, 67

Gallagher, P. T., Lawrence, G. R., & Dennis, B. R. 2003, ApJ, 588, L53

Galvin, A. B. 1997, Coronal Mass Ejections, AGU Monograph 99, 253

Gibson, S. E., & Low, B. C. 1998, ApJ, 493, 460

Gilbert, H. R., Holzer, T. E., Burkepile, J. T., & Hundhausen, A. J. 2000, ApJ, 537, 503

Gosling, J. T., Birn, J., & Hesse, M. 1995, Geophys. Res. Lett., 22, 869

Hayes, A. P., Vourlidas, A., & Howard, R. A. 2001, ApJ, 548, 1081

Hirayama, T. 1974, Sol. Phys., 34, 323

Hundhausen, A. J. 1999, in The Many Faces of the Sun, ed. K. Strong, J. Saba, B. Haisch, & J. Schmelz (New York: Springer), 143

Illing, R. M. E., & Hundhausen, A. J. 1986, J. Geophys. Res., 90, 10951

Ko, Y.-K., Raymond, J. C., Lin, J., Lawrence, G., Li, J., & Fludra, A. 2003, ApJ, 594, 1068

Kopp, R. A. & G. W. Pneuman 1976, Sol. Phys., 50, 85

Krall, J., Chen, J., Duffin, R. T., Howard, R. A., & Thompson, B. J. 2001, ApJ, 562, 1045

Lepping, R. P., Jones, J. A., & Burlaga, L. F. 1990, J. Geophys. Res., 95, 11957

Linker, J. A., Mikic, Z., Riley, P., & Lionello, R. 2002, EOS Trans. AGU, 83, Spring Meet. Suppl. Abstract SH22D-02

Lundqusit, S. 1950, Ark. Fys., 2, 361

Lynch, B. J., Coles, W. A., & Sheeley, N. R. Jr. 2002, Geophys. Res. Lett., 29, 19, 1913, doi:10.1029/2001GL014152

Lynch, B. J., Zurbuchen, T. H., Fisk, L. A., & Antiochos, S. K. 2003, J. Geophys. Res., 108, A6, 1239, doi:10.1029/2002JA009463

MacNeice, P. J., Antiochos, S. K., Phillips, A., Spicer, D. S., DeVore, C. R., & Olson, K. 2004, ApJ, In press

MacNeice, P. J., Olson, K. M., Mobarry, C., de Fainchtein, R., & Packer, C. 2000, Comp. Phys. Commun., 126, 330

Magara, T., Mineshige, S., Yokoyama, T., & Shibata, K. 1996, ApJ, 466, 1054

Manchester, W. B., IV, Gombosi, T. I., Roussev, I., De Zeeuw, D. L., Sokolov, I. V., Powell, K. G., Tóth, G., & Opher, M. 2004a, J. Geophys. Res., 109, A01102, doi:10.1029/2002JA009672

Manchester, W. B., IV, Gombosi, T. I., Roussev, I., Ridley, A., De Zeeuw, D. L., Sokolov, V., Powell, K. G., & Tóth, G. 2004b, J. Geophys. Res., 109, A02107, doi:10.1029/2003JA010150

Manoharan, P. K., & Kundu, M. R. 2003, ApJ, 592, 597

Martin, S. F. 1998, Sol. Phys., 182, 107

Marubashi, K. 1997, in Coronal Mass Ejections, Geophysical Monograph 99, ed. N. Crooker, J. A. Joselyn, & J. Feynman (Washington, DC: AGU), 147

Mikic, Z. & J. A. Linker, 1994, ApJ, 430, 898

Moore, R., et al. 1980, Solar Flares, Skylab Workshop II Monograph, ed. P. Sturrock (Boulder: Colorado University Press), 341

Odstrcil, D., Linker, J. A., Lionello, R., Mikic, A., Riley, P., Pizzo, V. J., & Luhmann, J. G. 2002, J. Geophys. Res., 107, 1493

Parker, E. N. 1963, Interplanetary Dynamical Processes (New York: Interscience)

Petschek, H. E., 1964, in Proc. AAS-NASA Symp., The Physics of Solar Flares, ed. W. N. Hess (NASA SP-50; Washington, DC: NASA), 425

Plunkett, S. P., et al. 2000, Sol. Phys., 194, 371

Riley, P., et al. 2003, J. Geophys. Res., 108, A7, 1272, doi:10.1029/2002JA009820

Riley, P., et al. 2004, J. Atmosph. Solar-Terrestrial Phys., in press

Rust, D. M. 1994, Geophys. Res. Lett., 21, 241

Sheeley, N. R. Jr., Walters, J. H., Wang, Y.-M., & Howard, R. A. 1999, J. Geophys. Res., 104, 24739

Shibata, K., S. Nozawa, & R. Matsumoto 1992, PASJ, 44, 265

Somov, B. V., & Kosugi, T. 1997, ApJ, 485, 859

Sterling, A. C., & Moore, R. M. 2001, ApJ, 560, 1045

——. 2004, ApJ, 602, 1024

Sturrock, P. A. 1968, in Structure and Development of Solar Active Regions, IAU Symp., 35, ed. K. O. Kiepenheuer (Dordrecht: Reidel Pub.), 471

——. 1980, Solar Flares, Skylab Workshop II Monograph (Boulder: Colorado University Press)

Sweet, P. A. 1958, Electricmagnetic Phenomena in Cosmical Physics, IAU Symp., 6, ed. B. Lehnert (Cambridge: Cambridge Univ. Press), 123

van de Hulst, H. C. 1950, Bull. Astron. Inst. Neth., 11, 135

van Driel-Gesztelyi, L., Wiik, J. E., Schmieder, B., Tarbell, T., Kitai, R., Funakoshi, Y., & Anwar, B. 1997, Sol. Phys., 174, 151

Wang, H., Qiu, J., Jing, J., & Zhang, H. 2003, ApJ, 593, 564

Welsch, B. T., Abbett, W. P., Fisher, G. H., & Regnier, S. 2004, ApJ preprint doi:10.1086/421767

Wu, S. T., Guo, W. P., Michels, D. J., & Burlaga, L. F. 1999, J. Geophys. Res., 104, 14789

Yokoyama, T., & Shibata, K., PASJ, 48, 353

Zhang, J., Dere, K. P., Howard, R. A., Kundu, M. R., & White, S. M. 2001, ApJ, 559, 452

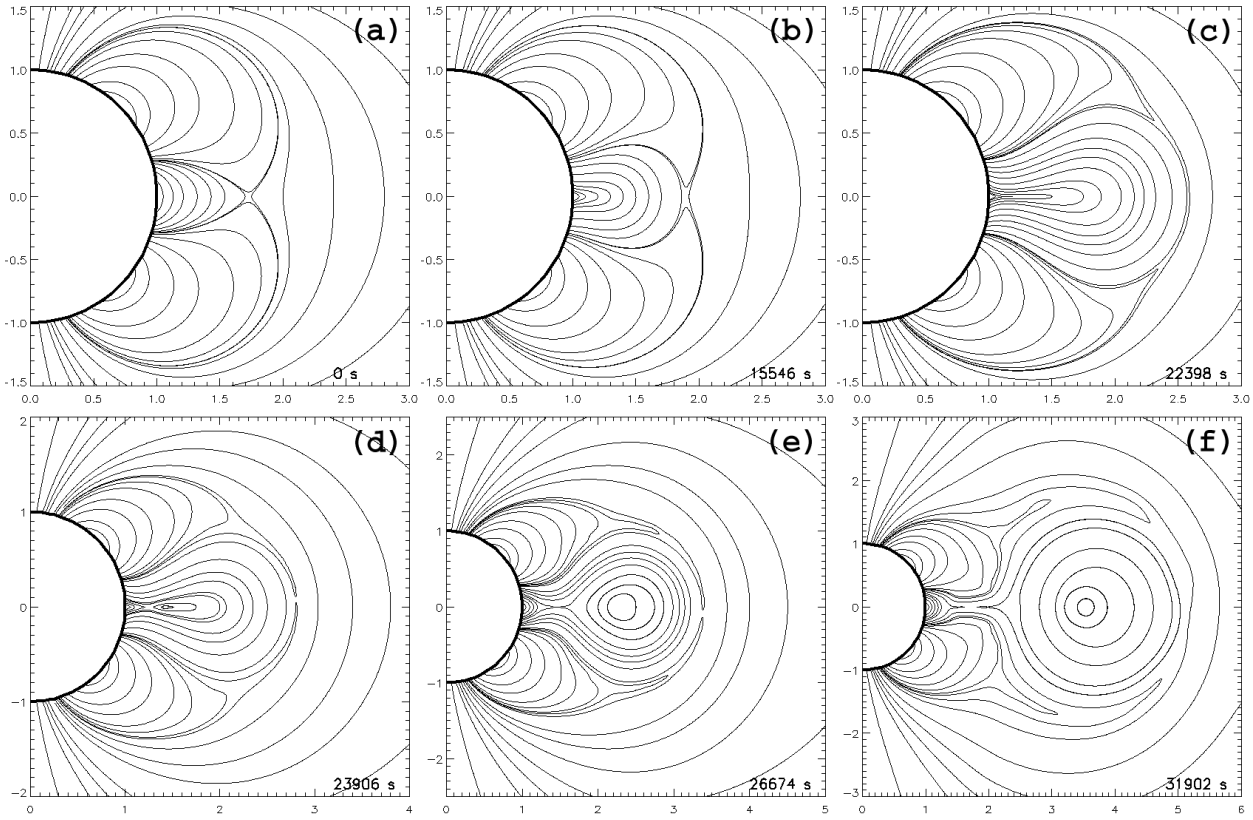

Fig. 1.— Meridional projections of magnetic fieldlines throughout the magnetic breakout eruption process. The overlying X-point is distorted into a current sheet allowing fast magnetic reconnection which triggers positive feedback between the sheared flux expansion and the removal of the overlying restraining flux. A current sheet forms beneath the erupting sheared field, creating a disconnected flux rope that escapes, as well as closing the remaining field back down to a more potential state. The axis units are $R_\odot$ and each panel indicates the elapsed simulation time.

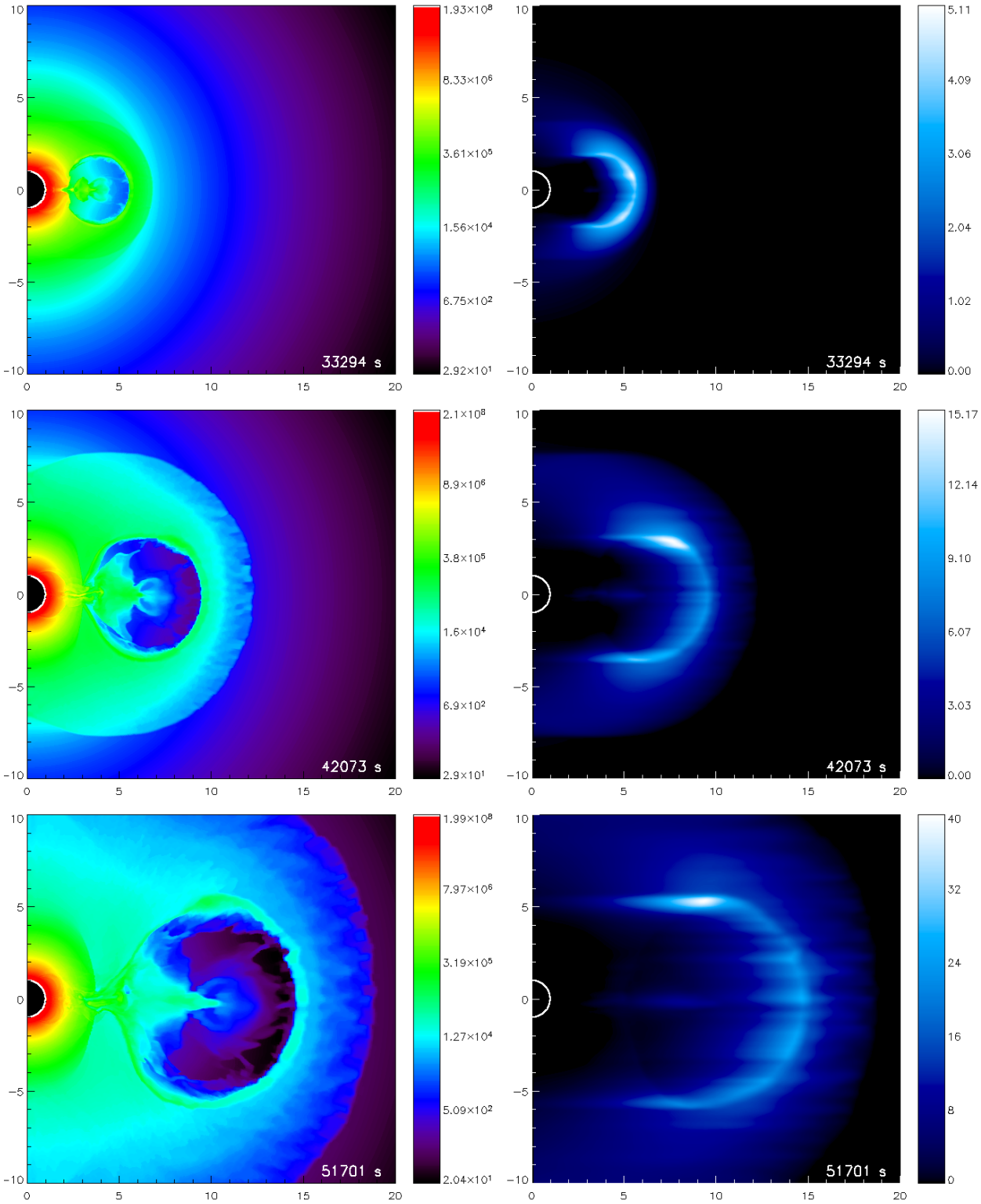

Fig. 2.— The left column images are number density [cm^{-3}] during the breakout simulation, showing the 3-part density structure. The right column shows the relative total brightness (equation 4) for the corresponding density plot. Due to background subtraction, the initial (snow-plowed) density enhancement has the largest response in the brightness images. The axis units are $R_\odot$ and each panel indicates the elapsed simulation time.

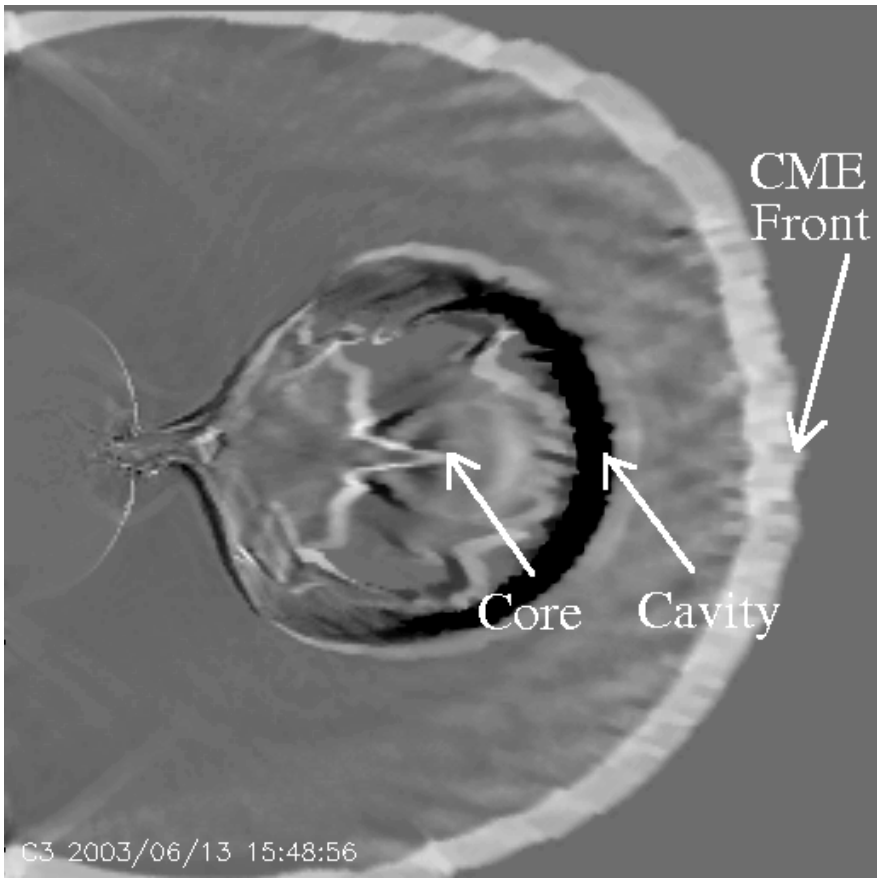

Fig. 3.— A contrast-enhanced running difference image from the breakout density movie. The arrows indicate the leading edges of the bright CME front, the dark cavity, and the central core region. The height-time profiles of these features are plotted in figure 4. The field of view is the same 20 $R_\odot$ box as the figure 2 panels, and the time stamp merely indicates the date of analysis and the elapsed simulation time.

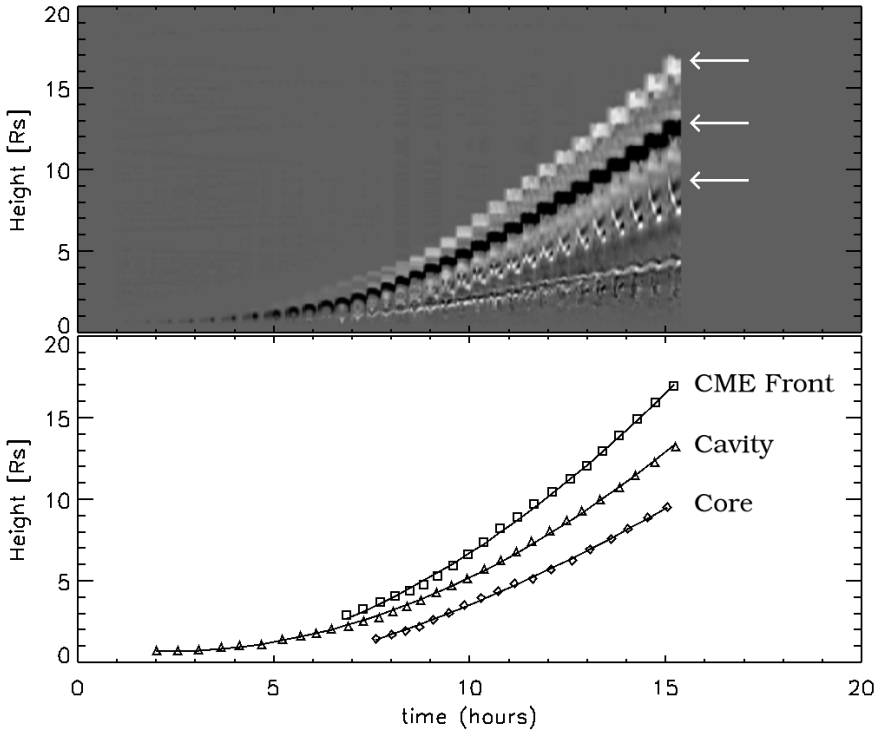

Fig. 4.— The top panel is the simulation height-time figure from the LASCO data analysis routines (cf. figures 1b, 3b of Sheeley et al. 1999). The arrows denote the tracks for each of the three running-difference features labeled in figure 3. The bottom panel shows the data points from the simulation and the solid lines are constant acceleration fits, with parameters listed in the text. While all three curves have the characteristic shape of the most common height-time profile for 3-part CMEs, we note that the CME Front reaches the Alfven speed of the numerical simulation, therefore these represent "fast" CME eruption speeds.

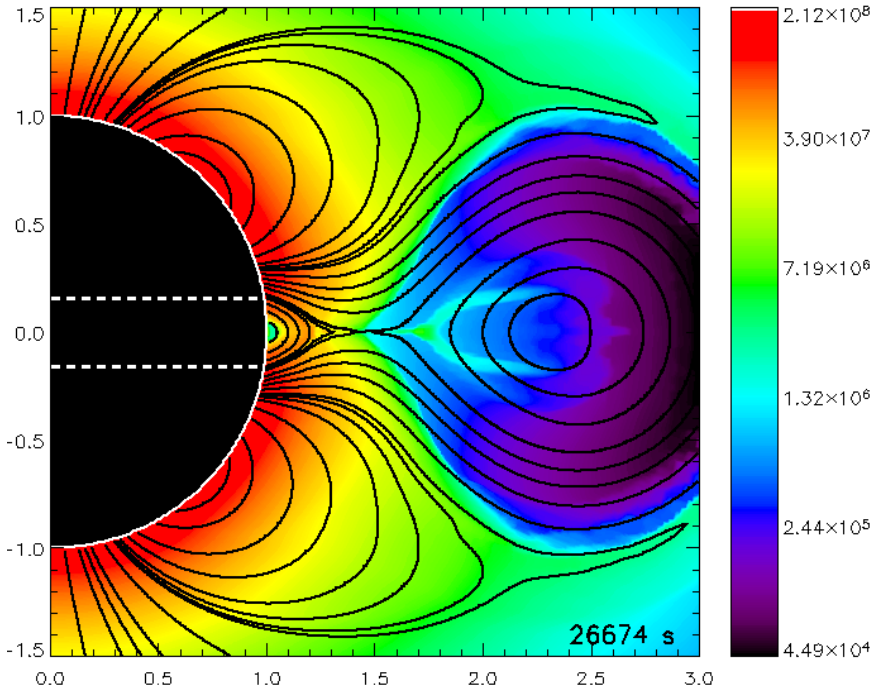

Fig. 5.— The meridional projection of fieldlines showing the current sheet formation underneath the breakout ejecta are plotted over the number density [cm^{-3}] in colorscale. The location of the azimuthally symmetric two-ribbon flare is plotted as the dashed line on disk center. The axis units are $R_{\odot}$ and the elapsed simulation time is shown at lower right.

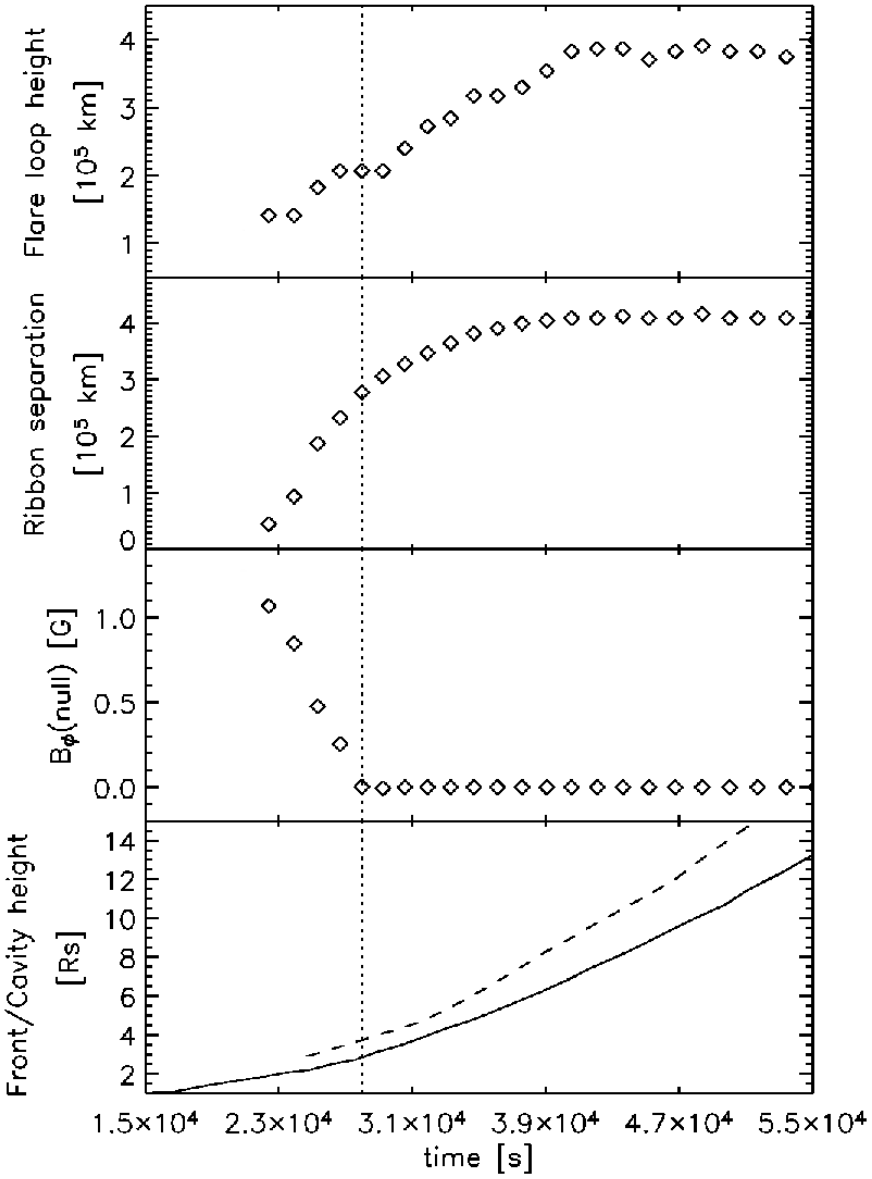

Fig. 6.— The post-eruptive flare loop height and flare-ribbon separation are plotted along with the B_ϕ value at the disconnection current sheet null-point and the height-time curves of the CME Front (dashed) and Cavity (solid) features from figure 4. The dotted vertical line indicates the end of reconnection with a shear component. We note that this appears to correspond to the transition from fast-to-slow footpoint separation and approximately to the end of the growth phase of the flux rope at ∼28,000 s (between (e) and (f) of figure 1).

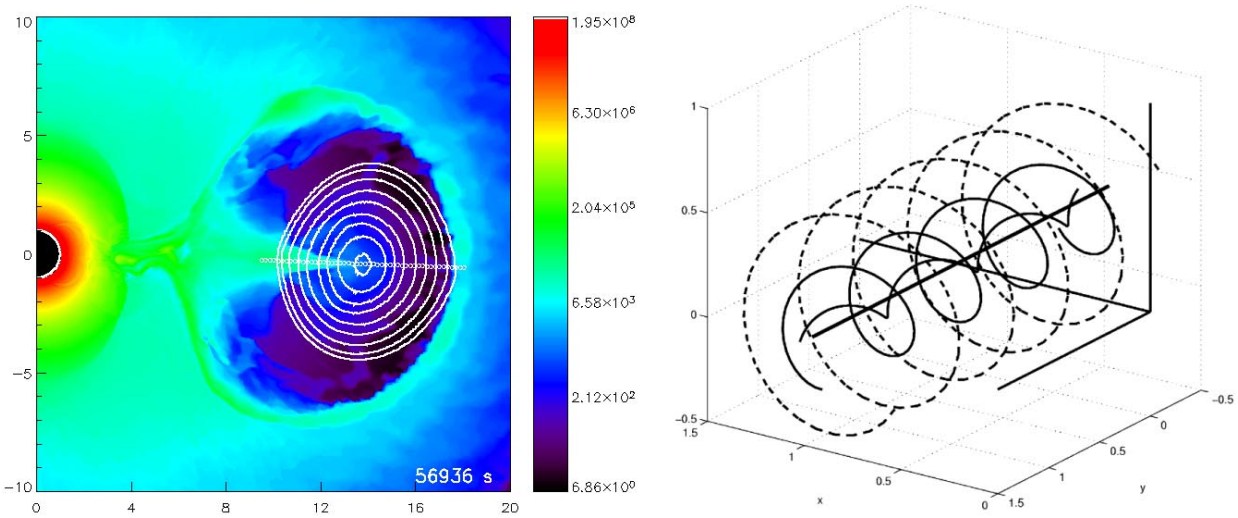

Fig. 7.— The left panel shows the projection of the flux rope magnetic field lines over the number density in the same format as the previous figures. The line of points represents the spatial sampling of the internal flux rope magnetic field structure, plotted in figure 8. The right panel plots representative field lines describing the structure of the linear, force-free cylinder model for magnetic cloud/flux-rope ICMEs, also plotted in figure 8.

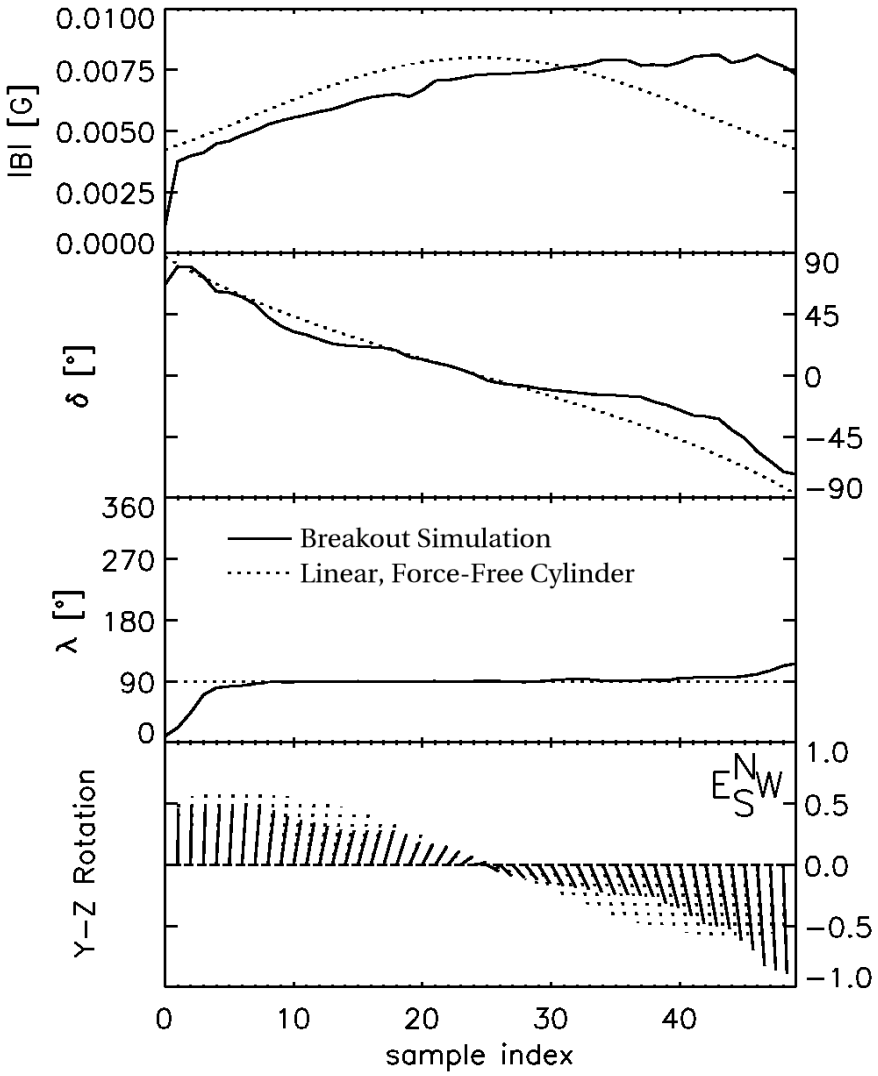

Fig. 8.— A comparison of the cylindrically symmetric, linear force-free model (dotted line) to simulation data samples (solid line) along the figure 7 cut. The first three panels are the magnetic field magnitude, latitude, and longitude. The LFF model has parameters, $\phi_0 = 90.0°, \theta_0 = 0°, \rho_0 = 0.0, H = -1, B_0 = 0.08$ G. The azimuthal angle and longitude are defined with respect to the positive x-direction (away from the sun), i.e. ϕ_0 of 90° gives positive $\hat{y}$ (toward the W limb), into the page. The fourth panel is the normalized field rotation in the y-z plane.

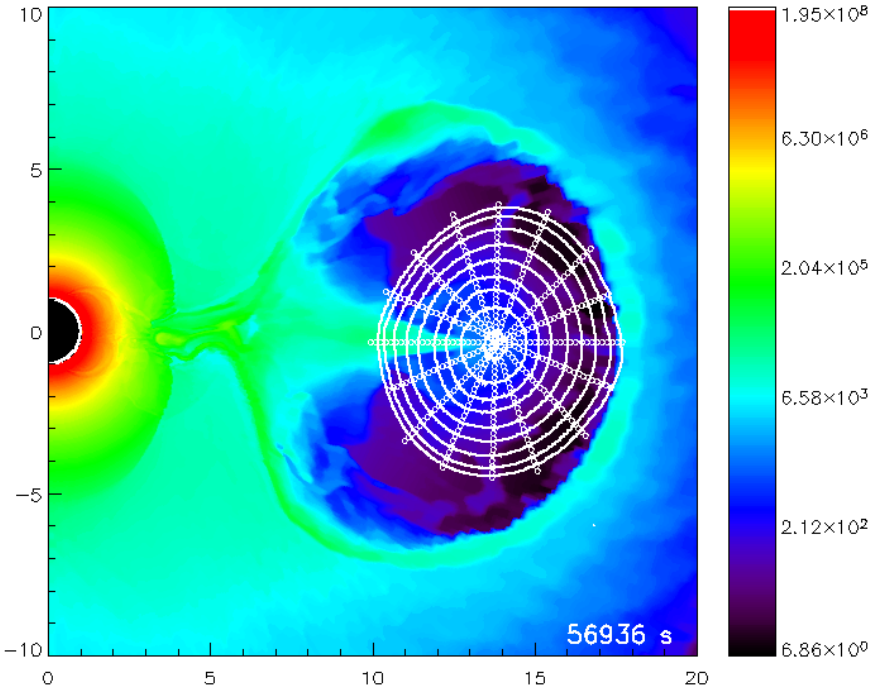

Fig. 9.— The 16 radial cuts used to construct the symmetric flux rope density average for comparison with 1 AU magnetic cloud observations in figure 10.

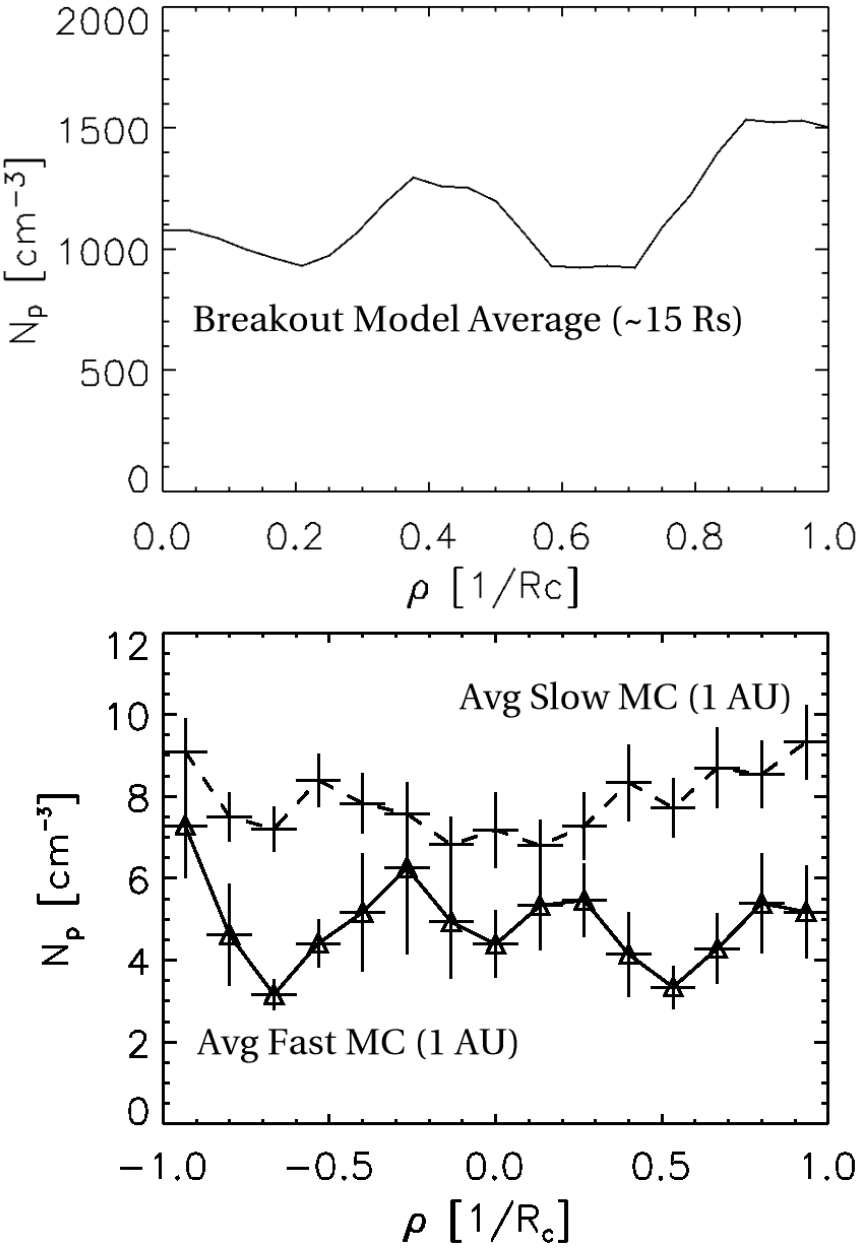

Fig. 10.— The top panel plots the average radial density profile of the breakout simulation flux rope derived from the cuts of figure 9. The simulation flux rope has an average radius of $R_c = 4.1$ R$_\odot$. The bottom panel shows the average diameter density profiles of "slow" and "fast" magnetic clouds at 1 AU, adapted from Lynch et al. (2003).